

Triton and Pluto

The long lost twins of active worlds
Adrienn Luspay-Kuti and Kathleen Mandt

Chapter 7

Magnetospheric and Space Environment Interactions with the Upper Atmosphere and Ionosphere

**Tom A Nordheim, Adrienn Luspay-Kuti, Lucas Liuzzo,
Peter Gao and G Randy Gladstone**

7.1 Introduction

Triton, with its retrograde and highly inclined orbit, is a likely captured Kuiper Belt Object (see Chapter 1). This places the moon in the same family as several dwarf planets in the Outer Solar System, most notably Pluto, whose orbital distance at perihelion is comparable to that of Neptune and Triton. Furthermore, these two icy worlds are of comparable size, mass, and density, and have extremely cold (\sim 30–40 K) surfaces rich in volatiles, including N₂, CH₄, and CO. Both worlds also possess tenuous but significant collisional atmospheres (Olkin et al. 2015; Strobel & Zhu 2017) sustained by volatile sublimation. However, unlike Pluto, Triton orbits within Neptune’s magnetosphere and is exposed to magnetospheric plasma and trapped energetic charged particles that precipitate into its upper atmosphere, providing an additional source of heating as well as ionizing atmospheric neutrals. This is highlighted by the fact that Triton’s ionosphere was found by *Voyager 2* to be surprisingly dense, while *New Horizons* failed to detect an ionosphere at Pluto. As the two worlds have similar solar inputs, this suggests that the magnetospheric charged particle input may be highly important at Triton. At the same time, *Voyager 2* detected a significant heavy ion component in Neptune’s magnetosphere, indicating that Triton is likely a significant source of plasma to Neptune’s magnetosphere. Neptune, its magnetosphere, and Triton’s upper atmosphere therefore represent a coupled system, and a holistic system-level approach will be required to further our understanding of the individual components. Furthermore, Neptune’s unusual tilted magnetic field leads to a complex and highly variable magnetospheric environment along Triton’s orbit, and the moon’s magnetospheric interaction was poorly constrained by the *Voyager 2* observations. These factors challenge our understanding of

the Neptune-Triton system. Here we will provide an overview of the upper atmospheres and ionospheres of Triton and Pluto, including the interaction of these objects with their respective space environments. We further discuss the possible role of magnetospheric particle precipitation as a dominant energy input at Triton, and compare its upper atmosphere and ionosphere to that of Pluto based on the new insights from the recent *New Horizons* flyby of the dwarf planet.

7.2 Neutral Atmospheres

Understanding how an atmosphere interacts with its environment requires knowledge of the neutral composition, surface temperature and pressure, ionospheric density and structure, sources of energy, and thermal structure as a function of distance from the surface. Limited information is available for Pluto and Triton, with the most valuable details provided by spacecraft measurements made during a single flyby of each. *Voyager 2* carried out a flyby of the Neptune system in 1989, measuring the composition and structure of the atmosphere and ionosphere of Triton using the *Voyager 2* Ultraviolet Spectrometer (UVS; Broadfoot et al. 1989) and Radio Science System (RSS; Tyler et al. 1989). *New Horizons* flew by Pluto in 2015 and measured the composition and structure of the atmosphere with the Alice Ultraviolet Spectrograph (Gladstone et al. 2016; Young et al. 2018) and determined an upper limit for the ionospheric density using the Radio Science Experiment (REX) (Hinson et al. 2018).

Both Pluto and Triton have atmospheres that are predominantly (>99%) N₂ with minor amounts of CH₄ and CO. At Triton, the atmosphere was found to have a very low CH₄ abundance of only ~0.01% during the *Voyager 2* flyby (Broadfoot et al. 1989; Herbert & Sandel 1991). Subsequent ground-based observations found that the CH₄ abundance had increased by ~4x in the time since the *Voyager 2* flyby, and also made the first measurement of CO in Triton's atmosphere at an abundance of 0.05%, similar to the surface CO ice abundance (Lellouch et al. 2010). At Pluto, the neutral atmosphere was measured during the *New Horizons* flyby to contain ~0.30% CH₄ (Young et al. 2018) and ~0.05% CO (Lellouch et al. 2017). Trace amounts of ethane (C₂H₆), acetylene (C₂H₂) and ethylene (C₂H₄) were also detected at Pluto with abundances on the order of 0.1% in the middle atmosphere but unexpectedly dropping to between 10⁻³ and 10⁻⁵% at ~100 km altitude (Young et al. 2018). These hydrocarbon species are likely also present at Triton (e.g., see discussion in Broadfoot et al. 1989), but have as of yet not been detected.

Pluto and Triton had similar surface temperatures during their respective space-craft flybys, 37±3 K (Gladstone et al. 2016) and 38⁺³₋₄ K, respectively. Both also had fairly low surface pressures of ~10 µbar for Pluto and ~14 µbar for Triton.

Energy input into an atmosphere determines the temperature profile and drives chemistry. Both Pluto and Triton receive energy from the Sun in the form of photons emitted at a broad range of wavelengths, from infrared through X-ray. They also receive energy from photons at Lyman-alpha wavelengths emitted by interstellar hydrogen emission (Bertaux & Blamont 1971) as well as from galactic cosmic rays. In addition to heating, these energy inputs also lead to dissociation and ionization of

the primary molecules in the atmosphere, leading to complex chemistry that eventually produces haze particles. This process is reviewed in detail in Chapter 6 of this book (Chapter 6). What is most notable is that very little haze was observed at Triton, extending only up to 30 km from the surface, while Pluto’s atmosphere was observed to have extensive layers of haze extending up to altitudes of at least 500 km.

Precipitating ions and electrons from the surrounding environment are also a source of energy for these atmospheres. Pluto interacts directly with the solar wind, which contains electrons as well as protons, alpha particles, and heavier ions with \sim eV to \sim keV kinetic energies. *New Horizons* observations of pickup ions originating from Pluto showed that methane was the primary molecule lost from the atmosphere at a rate similar to what is expected for Jeans escape (Bagenal et al. 2016). Triton, on the other hand, is located inside Neptune’s magnetosphere where magnetospheric ions and electrons with \sim eV to MeV energies precipitate into the upper atmosphere and may provide a significant energy source (e.g. Sittler & Hartle 1996).

Although both atmospheres have similar surface pressures and temperatures, the difference in methane abundance, a powerful greenhouse gas, and the additional source of energy from magnetospheric particle precipitation at Triton, leads to very different structures in the temperature profile of the two atmospheres. We compare Pluto and Triton based on the *New Horizons* (Gladstone et al. 2016) and *Voyager 2* (Krasnopolsky & Cruikshank 1995) observations in Figure 7.1, where the exobase is illustrated for both atmospheres using a dashed line. It is first notable that Pluto’s collisional atmosphere extends twice as far from the surface as Triton’s as a result of more efficient heating due to methane and other greenhouse gases, which is most effective at the lowest altitudes. By comparison, Triton’s atmosphere experiences the greatest heating in the upper atmosphere where magnetospheric particle precipitation provides an additional energy input.

7.3 Ionospheres

The only constraints available for the ionospheres of Triton and Pluto are from radio occultation measurements taken during the respective *Voyager 2* and *New Horizons* flybys. For both Triton and Pluto, near-terminator radio occultation measurements were taken on ingress and egress. While a very robust ionosphere was detected at Triton, *New Horizons* failed to detect any signature of an ionosphere at Pluto (Hinson et al. 2018). We illustrate these observations in Figure 7.2 and compare them with the predicted total electron density for Pluto’s atmosphere from modelling by Luspay-Kuti et al. (2017). The blue curve represents the predicted densities for an ionosphere at Pluto, which fall well below the lower detection limit of \sim 1000 cm $^{-3}$ for the *New Horizons* radio occultation experiment (blue shaded region). For comparison, the two ionospheric electron profiles returned by the *Voyager 2* radio science occultations of Triton are also included as the black curves. Finally, measured total ion densities for Titan from Mandt et al. (2012) are included as the yellow points. While Titan differs from Pluto and Triton in several key ways, it nonetheless represents another example of a cold upper atmosphere and

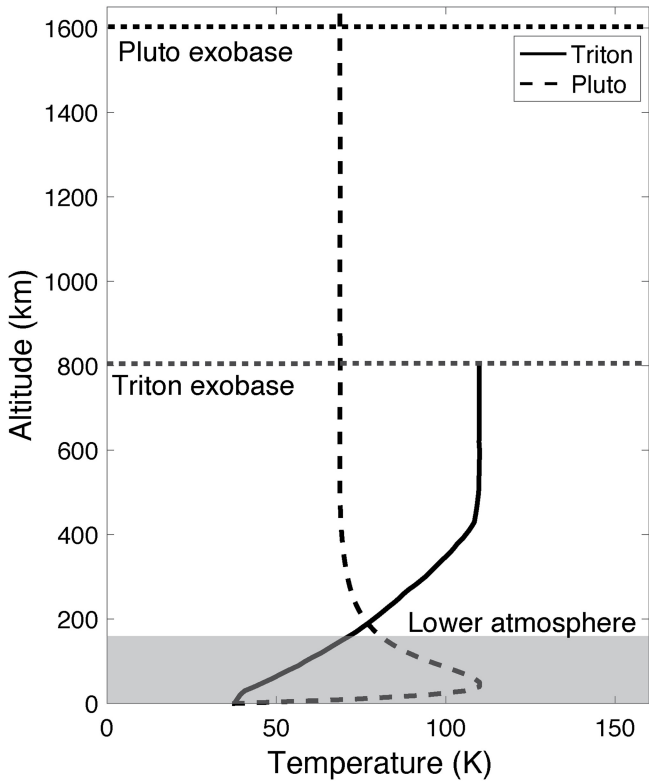


Figure 7.1. Temperature as a function of altitude for the atmospheres of Pluto (Gladstone et al. 2016; dashed) and Triton (Tyler et al. 1989; solid). The gray shaded area is the lower atmosphere. The upper atmosphere consists of the thermosphere and exosphere, which are separated by the exobase (thick dashed horizontal lines).

ionosphere dominated by nitrogen and hydrocarbon chemistry, with input from both solar photoionization and charged particle precipitation. From this comparison it becomes immediately obvious that Triton’s ionosphere stands out, with 1–2 orders of magnitude higher ionospheric electron densities than those at Pluto and Titan.

New Horizons carried out radio occultation measurements of Pluto’s atmosphere, at solar zenith angles of 90.2° (ingress, sunset) and 89.8° (sunrise, egress). No signature of an ionosphere was detected during these occultation measurements (Hinson et al. 2017, 2018). The instrument 1-sigma sensitivity was estimated to correspond to an integrated electron content (IEC) of $2.3 \times 10^{11} \text{ cm}^{-2}$, corresponding to a peak of ionospheric density in Pluto’s terminator region of no more than $\sim 1000 \text{ cm}^{-3}$. Hinson et al. (2018) constructed a simple ionospheric model for Pluto, predicting a peak IEC of $1.8 \times 10^{11} \text{ cm}^{-2}$, which is seemingly consistent with the non-detection of an ionosphere by the *New Horizons* REX. These authors argue that a key reason for the comparatively low ionospheric densities at Pluto is the higher abundance of CH₄ at ionospheric altitudes, leading to rapid removal of atomic ions through ion-neutral interactions with CH₄. The resulting molecular ions are readily

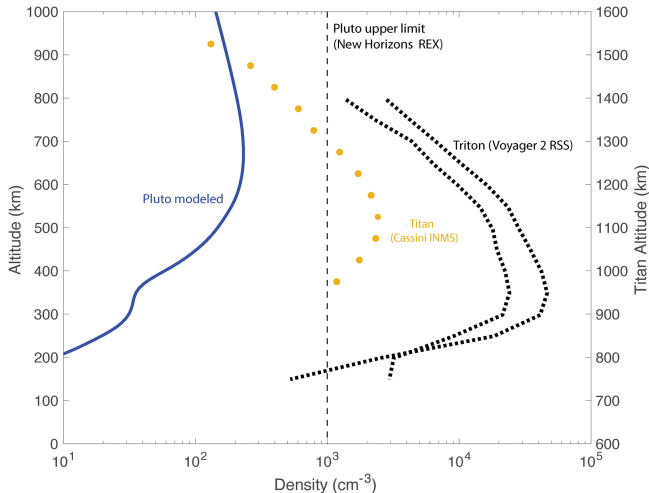


Figure 7.2. Altitude profiles of the electron densities observed at Triton by *Voyager 2* (black dashed lines; Tyler et al. 1989), the upper limit for Pluto’s ionosphere based on *New Horizons* (Dashed vertical line: Hinson et al. 2018). Predicted ionospheric electron densities at Pluto from Luspay-Kuti et al. (2017) are shown with the solid blue line to be well below the upper limit for ionospheric electron density determined by *New Horizons*. These are compared to the peak daytime ion densities measured by *Cassini* at Titan (Mandt et al. 2012, yellow points).

lost through dissociative recombination. Subsequent ionospheric modelling by Krasnapolsky (2020) predicted a maximum peak ionospheric density of $\sim 800 \text{ cm}^{-3}$, again consistent with the non-detection of an ionosphere at Pluto by *New Horizons*.

The radio occultation observations of Triton’s atmosphere and ionosphere by the *Voyager 2* RSS revealed that the Tritonian ionosphere is unusually dense ($n_e \sim 10^4 \text{ cm}^{-3}$) with an electron density peak located at $\sim 350 \text{ km}$ altitude (Tyler et al. 1989). The electron peak densities were measured as $\sim 2.3 \times 10^4 \text{ cm}^{-3}$ (350 km) and $\sim 4.6 \times 10^4 \text{ cm}^{-3}$ (340 km) during the RSS ingress and egress occultations, respectively (Figure 7.3). For comparison, this is comparable to, but somewhat larger than the electron densities in Callisto’s sunlit ionosphere ($\sim 1.5 \times 10^4 \text{ cm}^{-3}$) (Kliore et al. 2002) and much larger than those found in Titan’s ionosphere ($\sim 1\text{--}4 \times 10^3 \text{ cm}^{-3}$) (Kliore et al. 2008). This is surprising, as Triton receives a significantly lower flux of ionizing solar photons than these moons, e.g., a factor of $\sim 600\times$ and $\sim 400\times$, respectively.

Initial attempts at ionospheric modelling determined that the dominant ion in Triton’s ionosphere is N^+ , and that the ionospheric electron densities observed by *Voyager 2* RSS could only be reproduced when including magnetospheric electron precipitation as the major source of ionization (Ip, 1990; Lellouch et al. 1992; Majeed et al. 1990; Strobel et al. 1990; Yung & Lyons 1990). Weak EUV emissions from the sunlit hemisphere detected by *Voyager 2* UVS may also be consistent with significant magnetospheric electron precipitation (Broadfoot et al. 1989). However, subsequent modeling that included more coupled C-N chemistry proposed that it was possible to reproduce the magnitude and general structure of the Tritonian

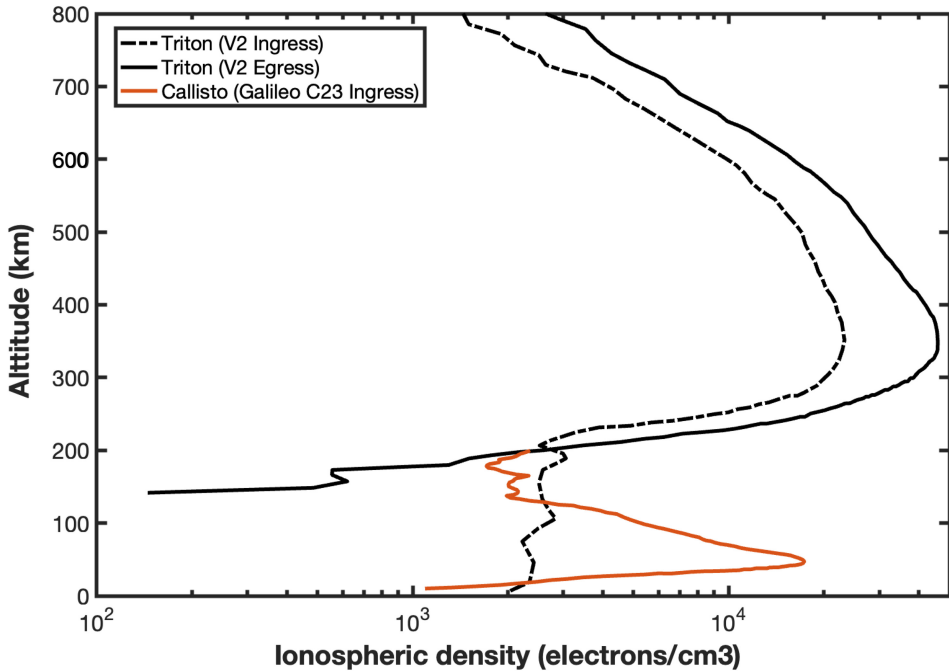


Figure 7.3. Total ionospheric electron number density at Triton as derived from Voyager 2 RSS occultations taken during the Voyager 2 flyby. Shown for comparison is the most intense ionospheric profile (C23 Ingress) observed by *Galileo* at Callisto in terms of peak electron densities. Adapted from Tyler et al. (1989) and Kliore et al. (2002).

ionosphere with solar EUV as the only major ionization source (Lyons et al. 1992). These authors suggested that C^+ , rather than N^+ , is the major ion in Triton's ionosphere assuming that charge exchange reaction $N_2^+ + C \rightarrow C^+ + N_2$ was taking place at very high reaction rates compared to similar type reactions. Krasnopolsky & Cruikshank (1995) used a lower rate more in line with similar type reactions and also found that C^+ was the dominant ionospheric species. However, they concluded that ionospheric chemistry at altitudes above 200 km is driven by solar EUV and magnetospheric electrons, requiring an energy input from magnetospheric electrons that is twice that from the solar EUV.

It was also noted that the observed thermospheric temperatures could not be produced by solar EUV alone, perhaps requiring additional input from magnetospheric electrons to explain the heating (e.g., Elliot et al. 2000; Stevens et al. 1992). More recently, Strobel & Zhu (2017) found that roughly equal amounts of solar EUV and magnetospheric particle heating are required to explain the neutral densities in Triton's atmosphere observed by *Voyager 2* UVS (Broadfoot et al. 1989), again indicating that magnetospheric particle precipitation plays an important role. Lellouch et al. (1992) determined that for Triton's ionosphere to be driven primarily by magnetospheric ion precipitation, the precipitating distribution would have to have a peak at unrealistically high energies (e.g., ~ 1.2 MeV). Thus, the

modelling studies in the literature have focused primarily on magnetospheric electron precipitation as an alternative (or complement) to solar photoionization.

It should be noted, however, that the reaction rate coefficient for the charge exchange reaction employed by Lyons et al. (1992) and Krasnopolksy & Cruikshank (1995) is highly uncertain. In order to generate the ionospheric densities observed by *Voyager 2* without magnetospheric input, the models by Lyons et al. (1992) required an unrealistically high rate coefficient for the charge exchange reaction producing C^+ . Using that coefficient, this model was able to reproduce the dense ionosphere by producing large amounts of C^+ , but failed to reproduce the profile of atomic N measured by the *Voyager 2* UVS between 170 km and 570 km (Krasnopolksy et al. 1993). Krasnopolksy & Cruikshank (1995) considered a total electron energy input based on thermal balance calculations, and concluded that an energy input from magnetospheric electrons that is 2–3 times higher than that from solar UV radiation is necessary to reproduce the measured atomic N profile.

Our understanding of ion-neutral chemistry has increased significantly since the *Voyager 2* era, and recent modeling for Pluto has indicated that the dominant ionospheric ions at Pluto are molecular ions: HCNH^+ above and $\text{C}_9\text{H}_{11}^+$ below the altitude of 600 km (Krasnopolksy 2020), with no indication that the $\text{N}_2^+ + \text{C} \rightarrow \text{C}^+ + \text{N}_2$ and other charge exchange reactions are important in Pluto's atmosphere. However, the relative importance of atomic and molecular ions in these atmospheres is predicted to depend strongly on the CH_4 surface mole fraction (Krasnopolksy 2012). These results suggest that at higher surface CH_4 mole fractions (e.g., induced by seasonal variations) Triton's ionosphere would transition to a different chemistry dominated by molecular rather than atomic ions (e.g. “*New Horizons* type” as termed by Krasnopolksy 2012). However, with only one ionospheric occultation measurement and no information on the actual ionospheric composition at Triton it is currently not possible to assess the validity of these predictions. An important clue would be if the change in seasons and increasing surface CH_4 mole fraction at Triton would also lead to a drop in the total ionospheric density, which would be expected from the hypothesis of Krasnopolksy (2012) if the chemistry were indeed mainly driven by photoionization.

Most recently, Benne et al. (2022) used the post-*Cassini* chemical scheme of Dobrijevic et al. (2016) developed for Titan and modified it by including association and charge exchange reactions from the early, *Voyager 2*-era studies. They also implemented the approach of Krasnopolksy & Cruikshank (1995) for the treatment of electron impact ionization, using the speculated ionization profiles from Strobel et al. (1990) and arbitrarily moving them up by two scale heights (e.g. as in Summers & Strobel 1991). Similarly, to Krasnopolksy & Cruikshank (1995), they also find that ionization by magnetospheric electrons is ∼2.5 times more important than photoionization in producing Triton's ionosphere. However, the predicted C^+ densities in their model is overproduced compared to the total electron density (or ion density, assuming charge neutrality) observed by *Voyager 2* radio occultations.

There is currently no clear consensus on whether Triton's ionosphere is predominantly driven by solar photoionization, magnetospheric charged particle precipitation, or some combination of the two. The large discrepancy between model

results highlights the many unknowns or poorly constrained parameters for Triton's neutral atmosphere, ionosphere, and magnetospheric charged particle input. Specifically, the model results are particularly sensitive to the assumed rate coefficient for the $\text{N}_2^+ + \text{C} \rightarrow \text{C}^+ + \text{N}_2$ charge exchange reaction. Reaction rate coefficients are generally poorly constrained at the low temperatures relevant to these outer planetary bodies, but the key charge exchange reaction that current photochemical models heavily rely on is almost completely unconstrained.

Another key aspect and major source of uncertainty is our understanding of precipitating magnetospheric charged particles to Triton's upper atmosphere and ionosphere. Some of the published modelling studies (e.g., Yung & Lyons 1990) approximated the magnetospheric energy contribution as a monoenergetic beam of electrons at the top of Triton's atmosphere. This approach does not consider the electron input as a function of energy, which is crucial because electrons of different energies lead to ionization at different altitudes in the atmosphere. Other studies (Ip, 1990; Lellouch et al. 1992; Sittler & Hartle 1996; Strobel et al. 1990) implemented an energy spectrum for the incident magnetospheric electrons at the top of the atmosphere. However, the overall flux and shape of this spectrum was poorly constrained by the *Voyager 2* measurements and was not consistent between the different studies, again likely contributing to the different model outcomes.

7.4 Pluto's Solar Wind Environment and Atmospheric Ion Escape

Pluto's interaction with its space environment is likely that of an unmagnetized body embedded within the solar wind. Thus, prior to the *New Horizons* flyby, it was predicted that Pluto may have a comet-style interaction, exemplifying a more extended obstacle, or a more compact Venus-like interaction (Bagenal et al. 2015, 2021; Bagenal & McNutt 1989). Firstly, the size of the interaction region depends strongly on the atmospheric escape flux. Secondly, it was realized that due to the low interplanetary magnetic field (IMF) strength at Pluto's heliospheric distance (~ 0.1 nT, Table 7.1), the gyroradii of heavy atmospheric pickup ions such as CH_4^+ and N_2^+ would be $\sim 10^2\text{--}10^3$ Pluto radii, many times larger than the region defined by Pluto's interaction with the Solar Wind. Thus, it is clear that kinetic effects are important, and that the Pluto interaction cannot be explained by a purely fluid-like (e.g. magnetohydrodynamic) picture (Delamere & Bagenal 2004). Prior to the *New Horizons* flyby, it was expected that, due to Pluto's low surface gravity, the neutral escape flux at the top of its atmosphere would be large, on the order of $10^{28}\text{--}10^{29}$ amu s⁻¹ (e.g., Zhu et al. 2014).

Pluto's upper atmosphere was found by *New Horizons* to be cooler and thus significantly more compact than expected, leading to an estimated atmospheric neutral escape rate of only $\sim 10^{27}$ amu s⁻¹ (Strobel & Zhu 2017; Gladstone et al. 2016; Hinson et al. 2017; Young et al. 2018). In addition to this substantially lower-than-expected atmospheric escape rate, the Solar Wind ram pressure was found to be significantly enhanced (by a factor of $\sim 3\times$) during the *New Horizons* encounter

Table 7.1. Representative Background (Upstream) Solar Wind Parameters Applicable to Pluto at a Heliospheric Distance of ~ 33 AU

	Predicted value at ~ 33 AU	Observed by <i>New Horizons</i>
Interplanetary magnetic field magnitude	0.08–0.28 nT	0.1–0.3 nT
Solar Wind proton density	0.0015–0.01 cm $^{-3}$	0.025 cm $^{-3}$
Solar wind proton temperature	0.16–1.5 eV	0.66 eV
Solar wind flow speed	340–480 km s $^{-1}$	403 km s $^{-1}$
Solar wind proton ram pressure	0.32–4.0 pPa	6.0 pPa
Alfven speed	22–96 km s $^{-1}$	14–41 km s $^{-1}$
Alvenic Mach number	4.6–20	9.8–29
Magnetosonic Mach number	5–17	9.5–23

The second column shows predicted values based on Voyager 2 heliospheric measurements and appropriate scalings from Bagenal et al. (2015). The third and last column lists the measurements made by the Solar Wind Around Pluto (SWAP) instrument onboard *New Horizons* at the time of the Pluto flyby (Bagenal et al. 2021; McComas et al. 2016). Note that the IMF strength was not directly measured as *New Horizons* did not carry a magnetometer, but rather inferred from SWAP observations and modelling.

with Pluto, likely due to the arrival of a strong interplanetary shock shortly before the encounter (see Table 7.1) (McComas et al. 2016). Thus, *New Horizons* and its Solar Wind at Pluto (SWAP) instrument observed the Pluto interaction region in a compressed state, which may not be representative of its state during typical quiescent solar wind conditions. McComas et al. (2016) estimated a solar wind standoff distance of only ~ 2.5 Rp during the encounter, with an estimated plutoopause boundary thickness of ~ 0.9 Rp (see Figure 7.4). Given the observed Solar Wind standoff distance and interaction region seen by *New Horizons*, it was possible to set an upper limit on Pluto's surface dipole magnetic field of < 30 nT, confirming that Pluto is an unmagnetized or only weakly magnetized body (McComas et al. 2016). SWAP observed Pluto to have a heavy ion tail that extended to at least 100 Rp downstream, with an estimated circular diameter of ~ 30 Rp at that distance. Furthermore, the SWAP observations indicated that the heavy ion tail is structurally variable with significant North-South asymmetries present. Zirnstein et al. (2016) argued that the detected plutogenic heavy ions were likely CH $_4^+$ and McComas et al. (2016) estimated a CH $_4^+$ escape rate of $\sim 8 \times 10^{24}$ amu s $^{-1}$, roughly 1% of the estimated neutral escape rate. Kollmann et al. (2019) reported on observations by the *New Horizons* Pluto Energetic Particle Spectrometer Science Investigation (PEPSSI), which indicated a surprisingly significant interaction between the Pluto obstacle and Interstellar Pickup Ions (IPIUs; pick-up ions generated by interstellar neutrals that penetrate the solar system), including an IPIU wake region that extended to a distance of ~ 190 Rp downstream of Pluto. Based on the *New Horizons* observations, it was concluded that Pluto's interaction with the

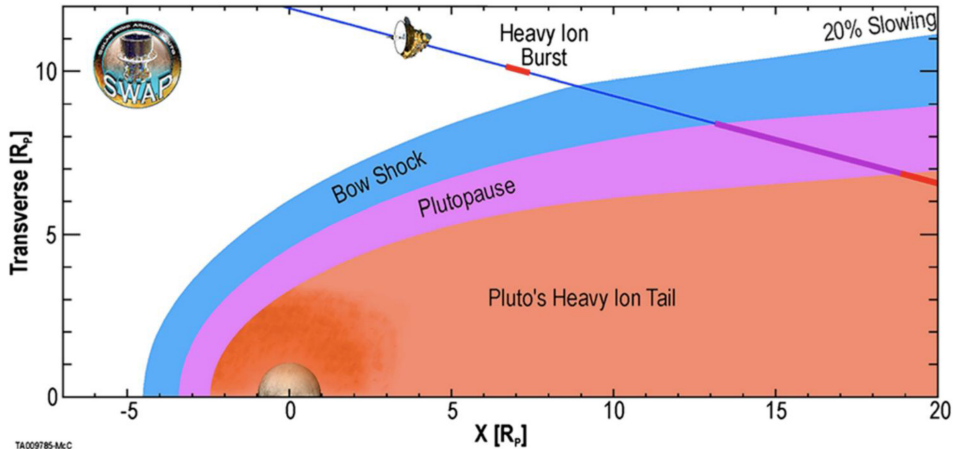


Figure 7.4. Schematic of the Pluto–Solar Wind interaction region as observed by *New Horizons* during its flyby. Reprinted with permission from Barnes et al. (2019).

solar wind is a hybrid of the predicted comet-like and Venus-like interaction modes, with the upstream bow shock generated by mass loading as is the case with comets, but the pressure balance diverting the shocked solar wind flow is sustained by atmospheric thermal pressure like it is at Venus (e.g., Bagenal et al. 2021 and references therein). Based on hybrid modeling Feyerabend et al. (2017) were able to reproduce the main characteristic features (e.g., location and thickness of the bow shock and plutoopause, heavy ion tail with significant N–S asymmetry) seen by *New Horizons* SWAP at Pluto. Hale & Paty (2017) carried out MHD simulations and found that the presence of Charon can significantly affect the morphology of the solar wind interaction region, and also partially shield Pluto from the solar wind when located upstream.

Barnes et al. (2019) compared hybrid simulations to SWAP observations during the *New Horizons* encounter and found that while in many respects, the solar wind interaction is similar to that of a weak comet, Pluto’s broad heavy ion tail is unique and shaped by the combination of the very low IMF and non-negligible thermal pressure provided by IPUIs.

The observations briefly summarized above indicate that Pluto displays a unique interaction with the solar wind, although possibly shared with other Kuiper Belt Objects, and many questions remain unanswered after the brief snapshot provided by the *New Horizons* flyby. In particular, the fact that the encounter appeared to coincide with significantly enhanced solar wind pressure indicates that the Pluto interaction region would be much larger in scale during quiescent solar wind conditions if the neutral escape rate stayed constant. Furthermore, it is expected that Pluto’s atmosphere varies significantly over seasonal and orbital timescales (Bertrand et al. 2019; Krasnopolsky 2020), likely also driving large changes in the neutral atmospheric escape rate and modifying Pluto’s interaction with the Solar Wind.

7.5 Neptune's Magnetospheric Environment and Triton's Role as a Possible Plasma Source

Neptune's magnetic field is highly tilted ($\sim 47^\circ$ for the dipole term) with respect to the planet's rotation axis. In combination with the large ($\sim 156^\circ$) orbital inclination of Triton relative to Neptune's rotational equator, this leads to a unique magnetospheric configuration very unlike that seen at, e.g., Jupiter and Saturn's satellites. Figure 7.5 illustrates the fact that Triton experiences a range of magnetic environments and magnetic field orientations, with Neptune's magnetic field lines in effect 'tumbling' over the moon across one Neptune synodic rotation. Triton orbits within a large range of magnetic L shells (the radial distance at which a given dipolar magnetic field line would cross the magnetic equator), from $L=14.3$ to 40 (Ness et al. 1989; Strobel et al. 1990). This also implies that Triton samples a diverse range of magnetospheric charged particle environments as it traverses the different regions of the Neptunian magnetosphere. Shown in Figure 7.6 is a plot of the magnetospheric plasma densities measured by *Voyager 2* during the inbound and outbound legs of its Neptune flyby organized by L-shell. While measurements at Triton's largest L-shell

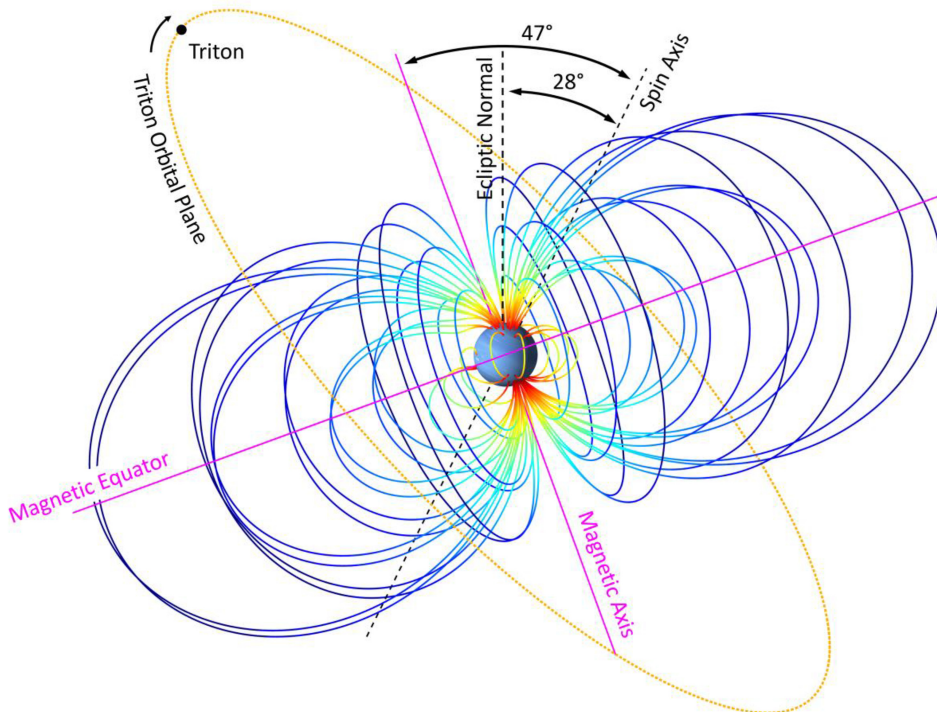


Figure 7.5. Illustration of the Neptune-Triton system, showing the tilt of Neptune's spin axis, the tilt of Neptune's magnetic axis with respect to its spin axis, the orbit of Triton and the magnetic equator populated with corotating plasma particles. Adapted with permission from Cochrane et al. (2022). CC BY-NC. See also Chapter 6 for a further discussion regarding Triton's interaction with Neptune's magnetic field.

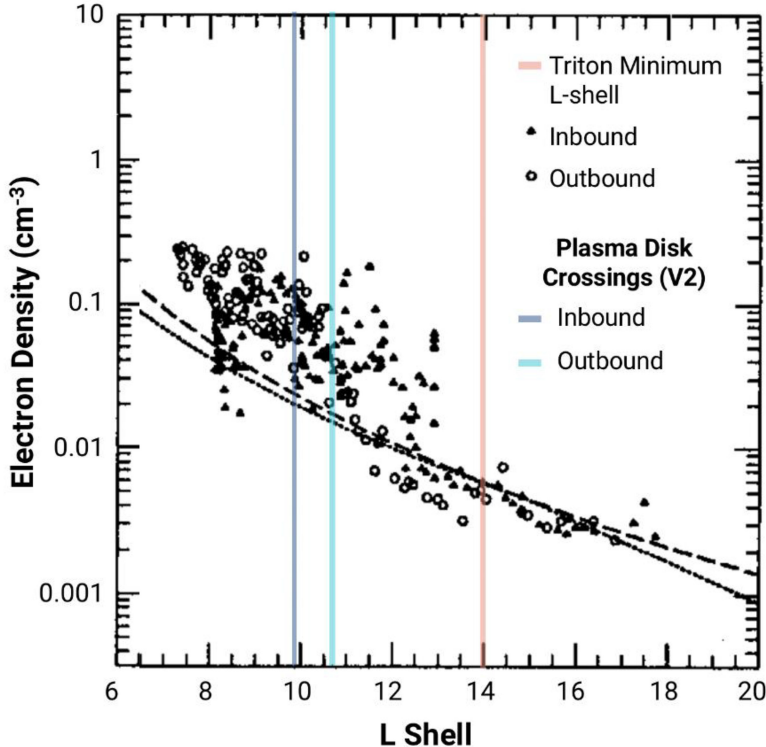


Figure 7.6. The magnetospheric electron density observed on the inbound (triangles) and outbound (circles) segments of the Voyager 2 flyby of Neptune. Observations are organized by magnetic L-shell from 6 to 20. The magnetic equator/plasma disk crossings are indicated for inbound and outbound. The dashed and dotted black lines are theoretically predicted plasma densities from two simple models (a constant flux shell model and a diffusion model), neither of which predict the actual densities well. Adapted with permission from Zhang et al. (1991).

excursions are lacking, this nonetheless demonstrates the inherent variability of the moon's ambient magnetospheric charged particle environment over the course of even a single synodic rotation. In addition to variations in the overall electron number density it is also conceivable, but currently not constrained by the observations, that the shape of the magnetospheric electron spectrum is also variable, e.g., as observed by *Cassini* at Titan (Rymer et al. 2009).

Our current best understanding of Triton's magnetospheric environment is based on measurements taken by *Voyager 2* around the time of its Triton flyby and summarized in Table 7.2 below. We emphasize that this was a distant flyby, where the closest approach to the moon was 39,800 km, and therefore the spacecraft never directly measured Triton's **local** magnetospheric environment. Furthermore, these numbers are representative of the ambient magnetospheric conditions during the flyby, when Triton was located near its **minimum** L-shell (~ 14) and are not necessarily applicable to Triton at other magnetic configurations. Therefore,

Table 7.2. Representative Background (Upstream) Magnetospheric Parameters Applicable to Triton During the *Voyager 2* Flyby, when the Moon was Located near L~14 in Neptune's Magnetosphere

Parameter	Value	Source
Background magnetic field magnitude	8 nT	Ness et al. (1989); Strobel et al. (1990)
Magnetospheric ion density	Total: $3 \times 10^{-3} \text{ cm}^{-3}$ H^+ : $1.5 \times 10^{-3} \text{ cm}^{-3}$ N^+ : $1.5 \times 10^{-3} \text{ cm}^{-3}$	Sittler & Hartle (1996); Zhang et al. (1991)
Magnetospheric ion temperature	H^+ : 16 eV N^+ : 100 eV	Richardson et al. (1991); Sittler & Hartle (1996)
Magnetospheric electron temperature	300 eV	Zhang et al. (1991)
Plasma flow speed relative to Triton	43 km s^{-1}	Strobel et al. (1990)
Plasma β	0.086	Sittler & Hartle (1996)
Alfven speed	1160 km s^{-1}	
Sound speed	95 km s^{-1}	
Alfvenic Mach number	0.037	
Sonic Mach number	0.45	

significant uncertainties exist regarding Triton's magnetospheric environment and the nature and strength of the magnetospheric electron precipitation source along Triton's full orbit.

Our best available estimate for the magnetospheric electron spectrum at Triton during the *Voyager 2* flyby is shown in Figure 7.7 (Sittler & Hartle 1996). This spectrum is derived from a Maxwellian fit to the *Voyager 2* Plasma Science Experiment (PLS; Zhang et al. 1991) and a power-law fit to measurements by the Low Energy Charged Particle Experiment (LECP; Krimigis et al. 1989; Mauk et al. 1991; Strobel et al. 1990) taken near Triton's minimum L-shell (L~14). Notably, there was a gap in measurement capability between the PLS and LECP instruments in the 6 to 20 keV range, so the magnetospheric electron spectrum is unconstrained in this region and populated by extrapolation.

Sittler and Hartle (1996) studied Triton's magnetospheric interaction and, based on analogies to Io and Venus, concluded that Triton's highly conductive ionosphere (Strobel et al. 1990) would likely stand off and divert the magnetospheric plasma flow, preventing a large fraction of magnetospheric electrons from reaching Triton's upper atmosphere and ionosphere. They estimated that a majority of $E < 2$ keV electrons would be diverted around Triton due to their $E \times B$ drifts and therefore not have access to the ionosphere, while only 30% of electrons with $E > 20$ keV would reach the ionosphere. This emphasizes that merely knowing the magnetospheric

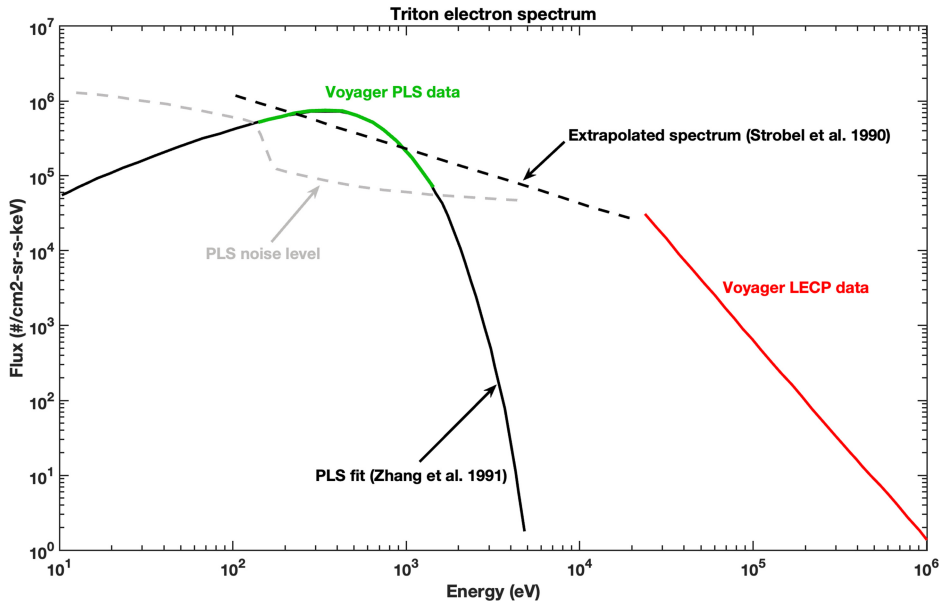


Figure 7.7. Current best estimate for the ambient magnetospheric electron spectrum at Triton during the *Voyager 2* flyby when Triton was located at $L \sim 14$. The green curve shows the part of the spectrum populated by a Maxwellian fit to the PLS measurements by Zhang et al. 1991 and the red curve shows a power-law fit derived from LECP measurements (Krimigis et al. 1989; Strobel et al. 1990). The two parts of the spectrum are separated by a measurement gap (blue shaded region) and joined by a simple straight-line extrapolation. Adapted with permission from Sittler & Hartle (1996).

electron spectrum near Triton is insufficient to understand the energy input to Triton's upper atmosphere. The spectrum of magnetospheric electrons precipitating at Triton will be determined by the moon's interaction with Neptune's magnetosphere and the perturbed local electromagnetic fields created as a response to this interaction.

Pre-encounter models predicted that Triton would be associated with a neutral/plasma torus (Delitsky et al. 1989). However, although the density of heavy ions in the Neptunian magnetosphere agrees reasonably well with the earlier model predictions, these ions were only observed during the plasma sheet crossings and not when *Voyager 2* crossed Triton's orbit (Belcher et al. 1989; Zhang et al. 1992). On the other hand, the inferred mass (10–40 amu, consistent with N^+) and average temperature (60–100 eV, consistent with pick-up at Triton's minimum L-shell) of the observed heavy ions is consistent with a Triton source. Belcher et al. (1989) calculated a pick-up energy of 120 eV for N^+ at rigid corotation. Cheng (1990) argued that Triton is the dominant source of plasma outside of $L \sim 7$ in the Neptunian magnetosphere and Sandel et al. (1990) suggested that a neutral source of $\sim 1 \text{ kg s}^{-1}$ from Triton's atmosphere could explain the observed power of the Neptunian aurora. Richardson et al. (1990) found that sputtering from Triton's atmosphere could produce the observed heavy ion densities at Triton's orbit if the

ion residence time is ~ 30 days. However, these authors also found that the Triton neutral source rate of $\sim 1 \text{ kg s}^{-1}$ from Sandel et al. (1990) is inconsistent with the *Voyager 2* PLS and UVS measurements. A subsequent study by Decker & Cheng (1994) found similar inconsistencies between the inferred plasma source rates and the predicted neutral escape rates from Triton's atmosphere. Measurements of hot plasma and energetic charged particles by the Voyager LECP instrument found that these populations appear to be strongly affected by Triton and/or interactions with the hypothetical Triton neutral torus (Mauk et al. 1991) and that a distinct trans-Triton heavy ion population exists outside the minimum L-shell of Triton. While Yung & Lyons (1990) concluded that the majority of nitrogen loss from Triton's upper atmosphere was in the form of direct ion escape, subsequent analyses by Richardson et al. (1990) and Summers & Strobel (1991) indicate that most of the nitrogen escaping Triton is in the form of neutrals. In this scenario, the magnetospheric N^+ ions would then be sourced from subsequent ionization of the torus neutrals and not locally at Triton.

7.6 Triton's Interaction with its Magnetospheric Plasma Environment

The time variability in the magnetospheric field near Triton's orbit drives currents in conducting layers at the moon that manifest as an induced magnetic field. These time-variable currents may be induced within a conductive, subsurface ocean, if it exists. Based on observations of the geologically young surface, Nimmo & Spencer (2015) have postulated that a global ocean could exist at depths below 200 km at Triton, sustained by tidal heating. However, the conductivity of such an ocean is poorly constrained. Besides a possible subsurface ocean, an additional conducting layer is Triton's ionosphere which is likely generated (at least in part) via precipitation of magnetospheric particles along the perturbed electromagnetic environment onto the moon's atmosphere. Given its high expected conductivities (e.g., Strobel et al. 1990), it is plausible that the time variability of the Neptunian magnetospheric field along the moon's orbit would drive currents within the ionosphere, which would manifest as an induced magnetic field detectable outside of the moon.

The combination of Triton's atmosphere, ionosphere, and induced magnetic field act as an obstacle to the impinging magnetospheric flow. Due to Triton's retrograde orbit ($\mathbf{u}_T \approx 4.4 \text{ km s}^{-1}$), the Neptunian magnetospheric plasma continually encounters the moon's orbital leading hemisphere at a relative velocity of $\mathbf{u}_0 \approx 43 \text{ km s}^{-1}$ (Strobel et al. 1990). As the plasma approaches Triton, it is diverted around the moon, generating perturbations in the plasma flow and electromagnetic fields near the moon. Figure 7.8 displays a schematic of Triton's electromagnetic environment for the case where the magnetospheric flow \mathbf{u}_0 is perpendicular to the background magnetic field \mathbf{B}_0 . Panel (a) is viewed against the direction of the convective electric field ($\mathbf{E}_0 = -\mathbf{u}_0 \times \mathbf{B}_0$), whereas panel (b) is viewed along the direction of the magnetospheric background field. Because the magnetospheric plasma along Triton's orbit is sub-Alfvénic (i.e., the Alfvénic Mach number $M_A = \frac{|v_A|}{|\mathbf{u}_0|} < 1$,

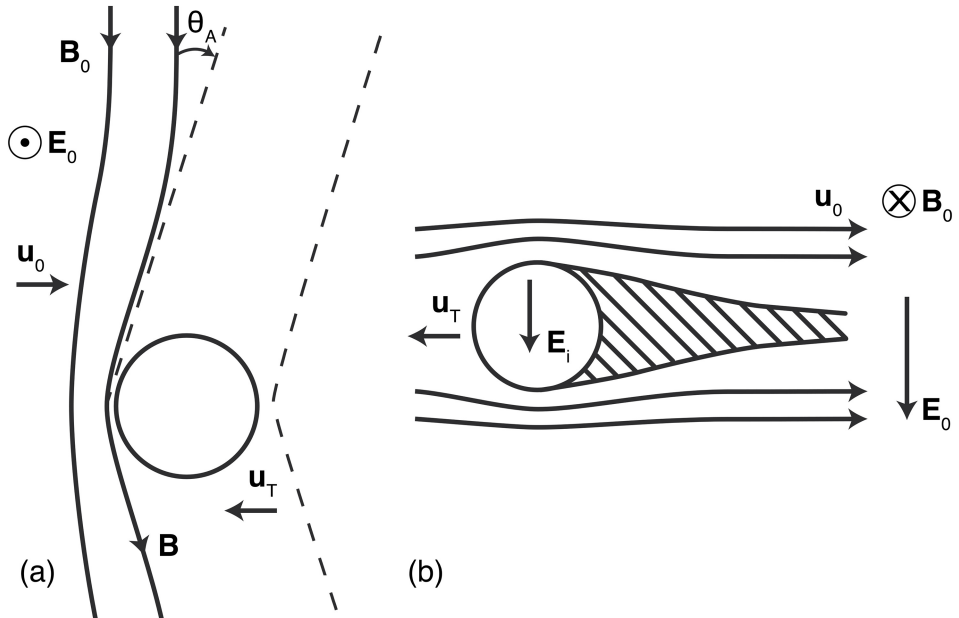


Figure 7.8. Schematic of an analytical model of Triton’s plasma interaction. Views are (a) looking against the convective electric field E_0 and (b) along the background magnetic field B_0 . Triton’s orbital motion is given by vector \mathbf{u}_T , magnetic field and flow streamlines are denoted by solid lines, and dashed lines illustrate the Alfvén characteristics. Adapted with permission from Strobel et al. (1990).

with Alfvén velocity v_A and magnetospheric plasma flow velocity \mathbf{u}_0 ; see Table 7.1), the moon’s interaction generates Alfvén wings that are inclined at an angle θ_A against the direction of the background magnetic field. These Alfvén wings—a system of nonlinear, standing Alfvén waves—connect Triton to Neptune’s ionosphere. The visual signature where these wings connect to Neptune’s ionosphere may be detected during future spacecraft missions to the ice giant, similar to the auroral footprints of the Galilean moons at Jupiter, or of Enceladus at Saturn. Shaded lines in Figure 7.8 denote the location of the moon’s plasma wake. Within Triton’s ionosphere, the electric field E_i is reduced below E_0 .

From an observational standpoint, the geometry of the Voyager 2 encounter was not ideal to detect signatures of Triton’s interaction with its magnetospheric environment. Closest approach of the spacecraft occurred nearly 40,000 km from the moon’s surface, and Neubauer et al. (1991) presented Voyager 2 magnetic field measurements during closest approach and noted an absence of any perturbations associated with Triton. Despite the lack of far-field observations, we can estimate how strongly the local convective electric field is reduced due to Triton’s interaction with the Neptunian magnetospheric plasma. By following the approach of Strobel et al. (1990) and Saur et al. (2013), we define an “interaction strength” parameter $\alpha = 1 - E_i/E_0$, where E_i represents the electric field within Triton’s ionosphere. For the case of no plasma interaction, this parameter reaches a value of $\alpha = 0$, while for

a strong interaction, α approaches a value of unity. This interaction strength parameter can be estimated via the equation:

$$\alpha = \frac{\Sigma_P}{\Sigma_P + 2\Sigma_A},$$

where Σ_P and Σ_A are the Pedersen and Alfvénic conductances, respectively (see also Neubauer 1980, 1998; Saur et al. 1999). At Triton, Σ_P exceeds 10^4 S (Strobel et al. 1990) while Σ_A is on the order of 1 S. Hence, Triton's interaction is “saturated” as the interaction strength reaches a value of $\alpha \approx 1$, and the electric field within the conducting ionosphere approaches $E_i \approx 0$ V m⁻¹. As a result, Strobel et al. (1990) estimated that streamlines of the magnetospheric plasma would be largely diverted around the moon (see discussion in 7.5 regarding consequences for magnetospheric particle precipitation).

However, this approach is only an estimate of how Triton's interaction perturbs its local environment: due to the low magnetic field along Triton's orbit, the typical magnetospheric and ionospheric ion gyroradii near Triton can approach the size of the moon. Hence, it is important to represent ion dynamics near the moon using a kinetic approach. One such study by Liuzzo et al. (2021) modeled Triton's interaction with the Neptunian plasma using a hybrid model, which accurately represents ion dynamics. Their goal was to determine how strongly Triton's plasma interaction could obscure the signature of an induced magnetic field at the moon. Liuzzo et al. (2021) found that for times during Triton's orbit when the magnetospheric field is perpendicular to the plasma flow direction, signatures of a magnetic field induced at Triton are likely detectable close to the moon's surface, even over the perturbations associated with the moon's plasma interaction. The weak electromagnetic fields associated with the moon's interaction for this scenario resemble those at the icy Galilean moons of Jupiter, where the magnetospheric field piles up and drapes around Triton's ionosphere and induced field, and generates a magnetic field enhancement upstream of the moon and an associated reduction in the total field magnitude within the wake. At greater distances from the moon, Alfvén wings form.

However, at times when the magnetospheric field forms an oblique angle to the flow direction, Liuzzo et al. (2021) found that Triton's interaction generates plasma interaction signatures that are unlike those observed at any other moon in the solar system. These authors identified a region of reduced magnetospheric plasma located downstream of Triton that resembled a typical absorption wake feature. However, the depletion was rotated out of the location of the expected wake (i.e., out of the geometric plasma shadow) by an angle similar to the angle formed between the magnetospheric field and plasma flow vectors (Figure 7.8). Liuzzo et al. (2021) illustrated that, for those times along Triton's orbit where \mathbf{u}_0 and \mathbf{B}_0 form an oblique angle to one another, one Alfvén wing characteristic (defined by $\mathcal{Z}_{0,\pm} = \mathbf{u}_0 \pm \mathbf{v}_{A,0}$; see Neubauer 1980) is located *upstream* of Triton. This causes the magnetospheric plasma to “ride” along the Alfvén wing located upstream and be diverted toward Triton. The resulting absorption of the plasma as it impinges onto Triton thereby causes an Alfvén wing absorption feature that is displaced out of the geometric plasma shadow. Such a signature has never been identified at any other solar system moon but may be a key feature of Triton's interaction.

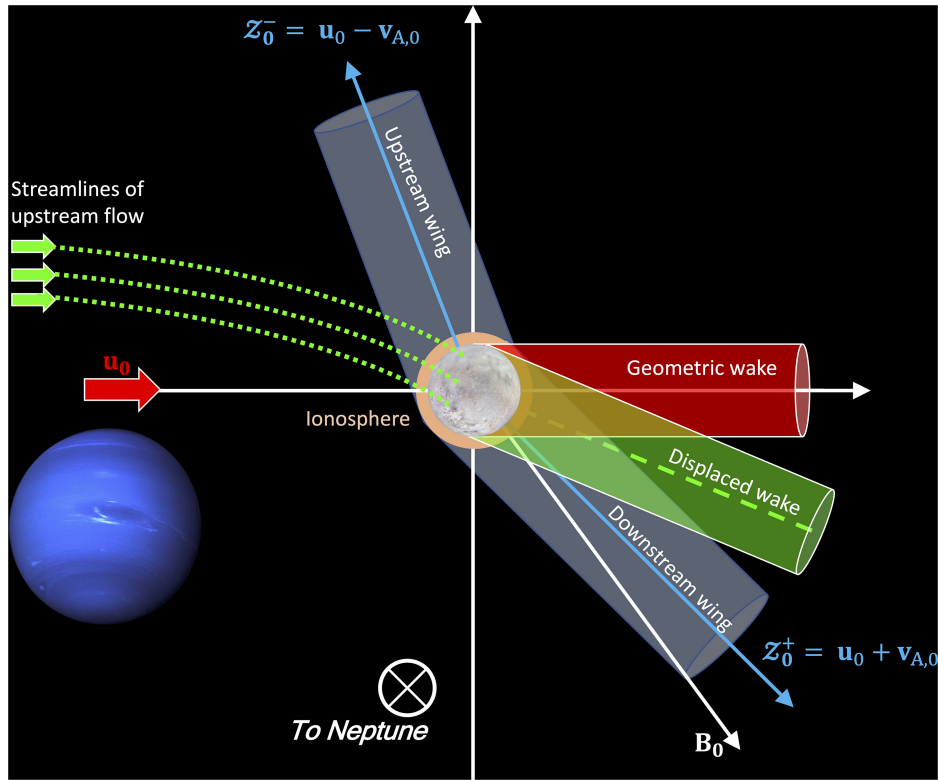


Figure 7.9. Schematic illustrating the geometry of Alfvén wings at Triton, for a case where the magnetospheric flow vector \mathbf{u}_0 forms an angle to the magnetospheric field \mathbf{B}_0 . When one wing is located upstream of the moon, the plasma flow is diverted toward Triton, generating a displaced plasma wake downstream of the moon that is tilted out of the geometric wake. Adapted with permission from Simon et al. (2022).

Recently, Simon et al. (2022) applied an analytical model to further understand these unique Alfvén wing absorption features associated with Triton’s plasma interaction. With their model, they placed constraints on the properties of the magnetospheric plasma required to generate such a feature at any moon. These authors identify a “critical angle” for flow deflection, whereby such a displaced wake would be formed by an Alfvén wing located upstream of a moon (Figure 7.9). They show that the “critical angle,” θ_c , satisfies $\sin \theta_c = M_A$. Simon et al. (2022) suggest that a similar feature could likely form at, e.g., exoplanets (see also Saur et al. 2013), the Uranian moons, or even at Saturn’s moon Titan (although the Cassini spacecraft did not observe this scenario during any of its encounters).

7.7 Conclusions

Triton and Pluto exhibit several strong similarities, with a likely shared origin in the Kuiper Belt. While the two objects both have cold and relatively dense $\text{N}_2\text{-CH}_4$ atmospheres with almost identical surface pressures, there are several key differences

between these twin worlds. Firstly, the neutral atmosphere of Pluto is much more extended than that of Triton due to the much larger fraction of CH₄ and other greenhouse gasses leading to low-altitude heating, and comparative studies of Pluto and Triton have yielded new insights into the role of atmospheric CH₄ at this class of object. Secondly, the two bodies reside in very different space environments, with Triton orbiting inside Neptune's magnetosphere while Pluto is almost certainly an unmagnetized body interacting directly with the solar wind and other heliospheric particle populations. Thus, respective flybys by *Voyager 2* and *New Horizons* found that the atmospheres, ionospheres, and space environment interactions of these two bodies are strikingly dissimilar.

Triton was found by *Voyager 2* to have a very dense ionosphere, with peak electron densities over an order of magnitude higher than those found at Saturn's moon Titan. This is also in strong contrast to Pluto, which hosts a very similar cold N₂-CH₄ atmosphere. At the time of the *New Horizons* flyby, Pluto was located at a similar solar distance as Triton, but radio occultations failed to detect any sign of an ionosphere above the *New Horizons* REX detection limit. This indicates that an additional energy source is at work in creating and maintaining Triton's unexpectedly dense ionosphere, likely precipitation of electrons from Neptune's magnetosphere. However, due to the limitations of the *Voyager 2* flyby dataset, it has not been possible to conclusively determine if Triton's ionosphere is primarily solar-driven or if magnetospheric electron precipitation plays a dominant role. A key aspect of this is the determination of the properties of magnetospheric electrons (energy spectrum, flux) incident on Triton, which has not been well constrained from the *Voyager 2* measurements. Furthermore, recent modelling has shown that Triton's plasma interaction with Neptune's magnetosphere may be complex and possibly of a type that is unique among solar system objects. This makes it more difficult to relate the properties of ambient (upstream) magnetospheric plasma to the population of electrons that precipitate at the top of Triton's atmosphere as these particles have first been altered by the perturbed local electromagnetic fields near the moon. Measurements by *Voyager 2* also indicate that Triton has an important role as a plasma source, providing a supply of heavy ions to Neptune's magnetosphere. However, the exact mechanism for atmospheric loss at Triton has not yet been conclusively determined, and while likely present, the long-hypothesized Triton neutral torus has not yet been confirmed by measurements.

The dwarf planet Pluto does not orbit within a magnetosphere and therefore interacts directly with the heliospheric environment determined by the interplanetary magnetic field, solar wind plasma, and local fluxes of interstellar pickup ions. *New Horizons* found that Pluto's solar wind interaction at the time of the flyby was a hybrid between that of a weak comet and an unmagnetized planet (e.g., Venus-like). In particular, it was found that while the overall large-scale interaction was comet-like, Pluto possessed a broad heavy ion tail that appeared to be a consequence of the low IMF and thermal pressure from IPUIs. The size of the Pluto interaction region was found to be much smaller than expected, primarily due to much lower rates of atmospheric neutral and ion escape than what was predicted before the flyby. Importantly, however, the *New Horizons* flyby coincided with a brief period of

enhanced solar wind pressure, likely leading to a more compressed solar wind interaction region than what would be observed under quiescent conditions. We now also understand that the Pluto–solar wind interaction is strongly controlled by the rate of neutral escape from its atmosphere. The neutral escape rate is tightly coupled to the state (e.g., temperature, structure, composition) of the atmosphere, which is expected to vary significantly over seasonal and orbital timescales. Thus, it is likely that the nature of the Pluto–solar wind interaction also varies over both short (e.g., solar wind variability) and long (orbital, seasonal) timescales. While *New Horizons* did not detect a robust ionosphere at Pluto during its encounter, it is plausible that the ionospheric state likewise also varies over time due to, e.g., changing atmospheric CH₄ mole fraction and possibly also differing contributions from heliospheric charged particle precipitation due to the changing nature of the solar wind interaction.

While we have individual snapshots in time from both the Neptune-Triton and Pluto systems, many questions remain unanswered, and it is clear that these worlds are highly dynamic, particularly with regards to their upper atmospheres and space environment interactions. Future missions to both systems, as well as to destinations within the Kuiper Belt are therefore warranted.

A New Frontiers class mission concept, the Triton Ocean World Surveyor, was highlighted by the recent 2023–2032 Decadal Strategy for Planetary Science and Astrobiology. If such a mission eventually goes forward, we emphasize that the exploration strategy should consider the fact that Neptune, its magnetosphere, and Triton’s upper atmosphere and ionosphere represent an inherently coupled system. For example, such a mission could determine the dominant energy input to Triton’s upper atmosphere and ionosphere, and investigate the mechanism and loss rates of neutrals and ions from Triton to Neptune’s magnetosphere by carrying out a combination of remote sensing and in-situ measurements in the Neptune-Triton system. Triton’s plasma interaction and magnetic induction response are also affected by the properties of the moon’s ionosphere and potential subsurface ocean, and therefore, an improved understanding of the upper atmosphere and its coupling to the magnetospheric environment will also aid in the future detection and characterization of a putative subsurface ocean on Triton.

A future mission to Pluto could investigate seasonal and orbital changes to its atmosphere, ionosphere, and surface volatiles that have occurred since the *New Horizons* flyby and determine whether a liquid subsurface ocean persists to present day. A dedicated Pluto orbiter could also investigate how Pluto’s solar wind interaction changes in response to solar wind and atmospheric variability, thus addressing one of the major open questions remaining after *New Horizons*. We should highlight that given the long orbital and seasonal timescales of these systems, further missions to both objects would be highly synergistic, even if they were somewhat spaced out in time.

References

- Bagenal, F., Delamere, P. A., Elliott, H. A., et al. 2015, *JGRE*, 120, 1497
 Bagenal, F., Horányi, M., McComas, D. J., et al. 2016, *Sci*, 351, aad9045

- Bagenal, F., McComas, D. J., Elliott, H. A., et al. 2021, The Pluto System After New Horizons, ed. S. A. Stern, et al. (Tuscon, AZ: Univ. Arizona Press) 379
- Bagenal, F., & McNutt, R. L. 1989, *GeoRL*, **16**, 1229
- Barnes, N. P., Delamere, P. A., Strobel, D. F., et al. 2019, *JGRA*, **124**, 1568
- Belcher, J. W., Bridge, H. S., Bagenal, F., et al. 1989, *Sci*, **246**, 1478
- Benne, B., Dobrijevic, M., Cavalié, T., Loison, J. C., & Hickson, K. M. 2022, *A&A*, **667**, A169
- Bertaux, J., & Blamont, J. 1971, *A&A*, **11**, 200
- Bertrand, T., Forget, F., Umurhan, O. M., et al. 2019, *Icar*, **329**, 148
- Broadfoot, A. L., Atreya, S. K., Bertaux, J. L., et al. 1989, *Sci*, **246**, 1459
- Cheng, A. F. 1990, *GeoRL*, **17**, 1669
- Cochrane, C. J., Persinger, R. R., Vance, S. D., et al. 2022, *E&SS*, **9**, e02034
- Decker, R. B., & Cheng, A. F. 1994, *JGR*, **99**, 19027
- Delamere, P. A., & Bagenal, F. 2004, *GeoRL*, **31**, 1
- Delitsky, M. L., Eviatar, A., & Richardson, J. D. 1989, *GeoRL*, **16**, 215
- Dobrijevic, M., Loison, J. C., Hickson, K. M., & Gronoff, G. 2016, *Icar*, **268**, 313
- Elliot, J. L., Strobel, D. F., Zhu, X., et al. 2000, *Icar*, **143**, 425
- Feyerabend, M., Liuzzo, L., Simon, S., & Motschmann, U. 2017, *JGRSP*, **122**, 10356
- Gladstone, G. R., Stern, S. A., Ennico, K., et al. 2016, *Sci*, **351**, aad8866
- Hale, J. P. M., & Paty, C. S. 2017, *Icar*, **287**, 131
- Herbert, F., & Sandel, B. R. 1991, *JGRA*, **96**, 19241
- Hinson, D. P., Linscott, I. R., et al. 2017, *Icar*, **290**, 96
- Hinson, D. P., Linscott, I. R., Strobel, D. F., et al. 2018, *Icar*, **307**, 17
- Ip, W.-H. 1990, *GeoRL*, **17**, 1713
- Kliore, A. J., Anabtawi, A., Herrera, R. G., et al. 2002, *JGRA*, **107**, 1407
- Kliore, A. J., Nagy, A. F., Marouf, E. A., et al. 2008, *JGRA*, **113**, A09317
- Kollmann, P., Hill, M. E., Allen, R. C., et al. 2019, *JGRA*, **124**, 7413
- Krasnopolsky, V. A. 2012, *P&SS*, **73**, 318
- Krasnopolsky, V. A. 2020, *Icar*, **335**, 113374
- Krasnopolsky, V. A., Sandel, B. R., Herbert, F., & Vervack, R. J. 1993, *JGR*, **98**, 3065
- Krasnopolsky, V. A., & Cruikshank, D. P. 1995, *JGR*, **100**, 21271
- Krimigis, S. M., Armstrong, T. P., Axford, W. I., et al. 1989, *Sci*, **246**, 1483
- Lellouch, E., Blanc, M., Oukbir, J., & Longaretti, P. Y. 1992, *AdSpR*, **12**, 113
- Lellouch, E., de Bergh, C., Sicardy, B., Ferron, S., & Käufl, H.-U. 2010, *A&A*, **512**, L8
- Lellouch, E., Gurwell, M., Butler, B., et al. 2017, *Icar*, **286**, 289
- Liuzzo, L., Paty, C., Cochrane, C., et al. 2021, *JGRA*, **126**, e29740
- Luspay-Kuti, A., Mandt, K., Jessup, K. L., et al. 2017, *MNRAS*, **472**, 104
- Lyons, J. R., Yung, Y. L., & Allen, M. 1992, *Sci*, **256**, 204
- Majeed, T., McConnell, J. C., Strobel, D. P., & Summers, M. E. 1990, *GeoRL*, **17**, 1721
- Mandt, K. E., Gell, D. A., Perry, M., et al. 2012, *JGRE*, **117**, 1
- Mauk, B. H., Keath, E. P., Kane, M., et al. 1991, *JGRA*, **96**, 19061
- McComas, D. J., Elliott, H. A., Weidner, S., et al. 2016, *JGRA*, **121**, 4232
- Ness, N. F., Acuna, M. H., Burlaga, L. F., et al. 1989, *Sci*, **246**, 1473
- Neubauer, F. M., Lüttgen, A., & Ness, N. F. 1991, *JGR*, **96**, 19171
- Neubauer, F. M. 1980, *JGRSP*, **85**, 1171
- Neubauer, F. M. 1998, *JGRP*, **103**, 19843
- Nimmo, F., & Spencer, J. R. 2015, *Icar*, **246**, 2

- Olkin, C. B., Young, L. A., Borncamp, D., et al. 2015, *Icar*, **246**, 220
- Richardson, J. D., Belcher, J. W., Zhang, M., & McNutt, R. L. 1991, *JGR*, **96**, 18993
- Richardson, J. D., Eviatar, A., & Delitsky, M. L. 1990, *GeoRL*, **17**, 1673
- Rymer, A. M., Smith, H. T., Wellbrock, A., Coates, A. J., & Young, D. T. 2009, *GeoRL*, **36**, L15109
- Sandel, B. R., Herbert, F., Dessler, A. J., & Hill, T. W. 1990, *GeoRL*, **17**, 1693
- Saur, J., Neubauer, F. M., Strobel, D. F., & Summers, M. E. 1999, *JGRSP*, **104**, 25105
- Saur, J., Grambusch, T., Duling, S., Neubauer, F. M., & Simon, S. 2013, *A&A*, **552**, 1
- Simon, S., Addison, P., & Liuzzo, L. 2022, *JGRA*, **127**, e29958
- Sittler, E. C., & Hartle, R. E. 1996, *JGR*, **101**, 10863
- Stevens, M. H., Strobel, D. F., Summers, M. E., & Yelle, R. V. 1992, *GeoRL*, **19**, 669
- Strobel, D. F., Cheng, A. F., Summers, M. E., & Strickland, D. J. 1990, *GeoRL*, **17**, 1661
- Strobel, D. F., & Zhu, X. 2017, *Icar*, **291**, 55
- Summers, M. E., & Strobel, D. F. 1991, *GeoRL*, **18**, 2309
- Tyler, G. L., Sweetnam, D. N., Anderson, J. D., et al. 1989, *Sci*, **246**, 1466
- Young, L. A., Kammer, J. A., Steffl, A. J., et al. 2018, *Icar*, **300**, 174
- Yung, Y. L., & Lyons, J. R. 1990, *GeoRL*, **17**, 1717
- Zhang, M., Belcher, J. W., & McNutt, R. L. 1992, *AdSpR*, **12**, 37
- Zhang, M., Richardson, J. D., & Sittler, E. C. 1991, *JGR*, **96**, 19085
- Zhu, X., Strobel, D. F., & Erwin, J. T. 2014, *Icar*, **228**, 301
- Zirnstein, E. J., McComas, D. J., Elliott, H. A., et al. 2016, *ApJ*, **823**, L30